LETTER

doi:10.1038/nature20801

A theoretical foundation for multi-scale regular vegetation patterns

Corina E. Tarnita[1,2]*, Juan A. Bonachela[3]*, Efrat Sheffer[4], Jennifer A. Guyton[1], Tyler C. Coverdale[1], Ryan A. Long[5] & Robert M. Pringle[1,2]

Self-organized regular vegetation patterns are widespread[1] and thought to mediate ecosystem functions such as productivity and robustness[2–4], but the mechanisms underlying their origin and maintenance remain disputed. Particularly controversial are landscapes of overdispersed (evenly spaced) elements, such as North American Mima mounds, Brazilian *murundus*, South African *heuweltjies*, and, famously, Namibian fairy circles[5–13]. Two competing hypotheses are currently debated. On the one hand, models of scale-dependent feedbacks, whereby plants facilitate neighbours while competing with distant individuals, can reproduce various regular patterns identified in satellite imagery[1,14,15]. Owing to deep theoretical roots and apparent generality, scale-dependent feedbacks are widely viewed as a unifying and near-universal principle of regular-pattern formation[1,16,17] despite scant empirical evidence[18]. On the other hand, many overdispersed vegetation patterns worldwide have been attributed to subterranean ecosystem engineers such as termites, ants, and rodents[3,4,7,19–22]. Although potentially consistent with territorial competition[19–21,23,24], this interpretation has been challenged theoretically and empirically[11,17,24–26] and (unlike scale-dependent feedbacks) lacks a unifying dynamical theory, fuelling scepticism about its plausibility and generality[5,9–11,16–18,24–26]. Here we provide a general theoretical foundation for self-organization of social-insect colonies, validated using data from four continents, which demonstrates that intraspecific competition between territorial animals can generate the large-scale hexagonal regularity of these patterns. However, this mechanism is not mutually exclusive with scale-dependent feedbacks. Using Namib Desert fairy circles as a case study, we present field data showing that these landscapes exhibit multi-scale patterning—previously undocumented in this system—that cannot be explained by either mechanism in isolation. These multi-scale patterns and other emergent properties, such as enhanced resistance to and recovery from drought, instead arise from dynamic interactions in our theoretical framework, which couples both mechanisms. The potentially global extent of animal-induced regularity in vegetation—which can modulate other patterning processes in functionally important ways—emphasizes the need to integrate multiple mechanisms of ecological self-organization[27].

Hypotheses about the origin of regularly patterned (that is, spatially periodic with characteristic cluster size) landscapes are typically presented as strict alternatives, leading to strident and long-lasting debates[5–12,17,22,28]. The Namibian fairy circles (FCs) provide a fascinating case in point. FCs are bare discs 2–35 m wide surrounded by rings of tall perennial grasses, found in sandy desert soils along a sliver of southwestern Africa[7,28] (Fig. 1f). Recently, Juergens[7] documented strong correlations between FCs and sand-termite (*Psammotermes allocerus*) activity and proposed a conceptual model in which termites engineer FCs by killing plants, thereby creating bare patches that concentrate moisture[7,8]. This hypothesis elicited a barrage of counter-arguments that FCs instead result from scale-dependent feedbacks (SDF)[9–13,18], with ensuing debate revolving heavily around the large-scale hexagonal distribution of FCs (each FC has approximately six neighbours on average). It has been argued, for example, that social insects 'are not able to create such extremely ordered, and at the same time large-scale, homogeneous patterns', leaving SDF as 'the most reasonable working hypothesis'[17]. Parallel disputes simmer over the origins of other regular vegetation patterns worldwide, pitting SDF against the activities of ants, termites, and other burrowing animals[5].

Although often implicitly presented as alternatives, these two mechanisms are not mutually exclusive. Here we reconcile these competing perspectives by theoretically integrating both mechanisms and testing their predictions against empirical observations. First, we develop a dynamic spatial model to characterize the population dynamics and territorial behaviour of a generic soil-nesting social-insect population, showing that intraspecific competition can generate the large-scale hexagonal patterns found in termite mounds[3], *heuweltjies*[22], *murundus*[5], and FCs[10]. Second, to explore the dynamic interaction and emergent effects of multiple simultaneous self-organization processes, we couple this faunal model to one of SDF-driven vegetation self-organization. We illustrate the power of this merged framework using Namibian FCs as a case study: by parameterizing our merged model specifically for that system and testing its predictions against remotely sensed imagery and field observations, we show that the interplay of both mechanisms (1) characterizes the vegetation patterns of Namibian FC landscapes more completely than either mechanism can in isolation, and (2) predicts the emergence of features in these landscapes that have escaped the notice of previous investigators. This analysis moves beyond dichotomous debates to explore the multi-trophic dynamics and feedbacks that underpin multi-scale regular patterning in complex ecosystems.

To model social-insect self-organization, we used a spatially explicit model of colony dynamics in a discrete landscape, parameterized from the literature (Extended Data Table 1). Colonies build central nests and forage outwards to acquire resources to fuel colony-population growth and survival. Mature (established) colonies produce alates (reproductive future queens/kings) that disperse randomly throughout our simulated landscapes and attempt to initiate new colonies. Resource availability is constant and uniformly distributed. When the expanding foraging areas of neighbouring colonies overlap, conflicts ensue via territorial aggression (Extended Data Fig. 1a), as is common in many social-insect species[29]. Conflict outcomes depend probabilistically on relative colony size: larger colonies are more likely to eliminate smaller ones, but similar-sized colonies coexist, whereupon a shared boundary emerges (Extended Data Fig. 1b). These conflicts are the primary cause of young-colony mortality (and are intensified by environmental

[1]Department of Ecology and Evolutionary Biology, Princeton University, Princeton, New Jersey 08544, USA. [2]Mpala Research Center, PO Box 555, Nanyuki, Kenya. [3]Marine Population Modelling Group, Department of Mathematics and Statistics, University of Strathclyde, Glasgow G1 1XH, Scotland, UK. [4]The Robert H. Smith Institute for Plant Sciences and Genetics in Agriculture, The Faculty of Agriculture, Hebrew University of Jerusalem, Rehovot 7610001, Israel. [5]Department of Fish and Wildlife Services, University of Idaho, Moscow, Idaho 83844, USA.
*These authors contributed equally to this work.

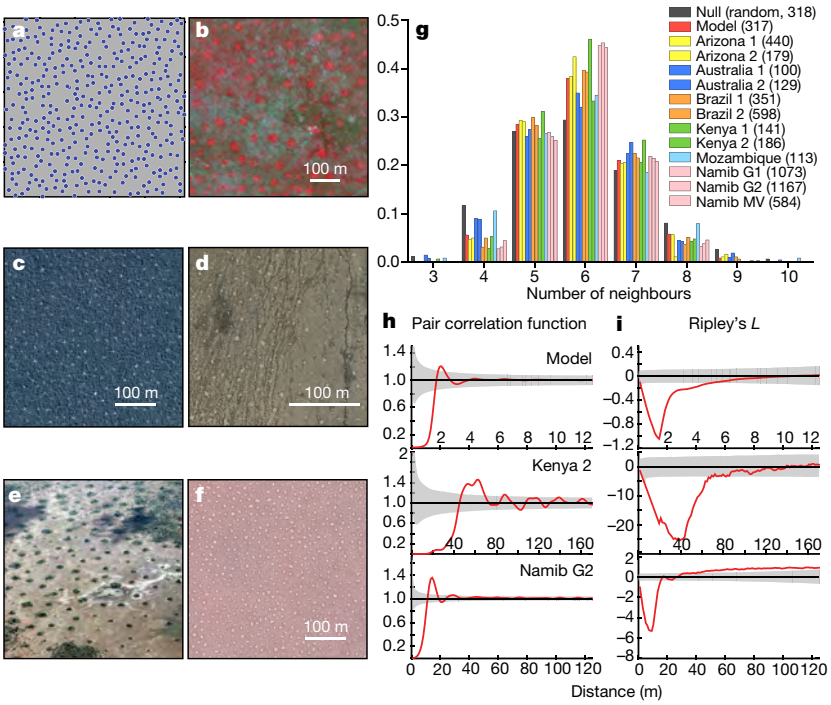

Figure 1 | Social-insect nest distributions, in theory and in nature. a, Model results: blue dots represent centres of mature nest sites; parameterization in Extended Data Table 1. See Supplementary Video 1 for model dynamics. **b**–**e**, Remotely sensed images of hexagonal termite and ant nests in (**b**) Kenya (false-colour composite from high-resolution multispectral satellite image; red spots, *Odontotermes montanus* mound locations); **c**, Brazil (pale dots, *Syntermes dirus* nests); **d**, Arizona, USA (bare circles, *Pogonmyrmex barbatus* nests); **e**, Mozambique (thicket clumps, *Macrotermes* sp. mounds). Features shown in **b**–**e** have been ground-truthed as social-insect nests (see Methods and Supplementary Information section 4.1). **f**, FCs in Namibia. **g**, Neighbour-number distributions from Voronoi-diagram analysis; bars left-to-right correspond to legend top-to-bottom. Numbers in parentheses correspond to numbers of nests analysed. **h**, **i**, Pair correlation and Ripley's *L* functions (red curves) for model results (top), Kenyan *Odontotermes* nests (middle), and Namibian FCs (bottom). Shaded areas represent 95% simulation envelopes to distinguish from complete spatial randomness. Details of images and analyses in Methods and Supplementary Information. Pleiades-1 satellite imagery in **b** copyright 2013 CNES/Astrium (GeoTIFF file supplied by Apollo Mapping, Boulder, Colorado, USA); Google Earth imagery in **c** copyright 2016 CNES/Astrium, **d** copyright 2012 DigitalGlobe, and **f** copyright 2016 DigitalGlobe; aerial photograph in **e** by R.M.P.

stressors such as drought), while mature colonies have an additional probabilistic death rate consistent with typical lifespans reported in the literature.

Although this system is intrinsically dynamic owing to continual births and deaths of colonies (Supplementary Video 1), the quantities of interest eventually reach stationarity (fluctuating around a well-defined constant average) (Extended Data Fig. 2a, b). We can thus explore how this stationary state depends on resource availability. Mean density and population size of mature colonies increased—and mean nest diameter, foraging area, and nearest-neighbour distance decreased—with increasing resource density (Extended Data Fig. 2c–f). This occurred because colonies in resource-rich environments require smaller foraging areas to achieve a given increase in population size. Moreover, colony sizes in low-resource environments were always food-limited (Extended Data Fig. 2f), consistent with previous experimental work[20].

We quantified predicted nest distributions (Fig. 1a) using standard point-pattern analyses: Voronoi diagrams, Ripley's *L* and pair correlation functions (see Methods). Regardless of resource density, mature nests in our simulations were regularly and hexagonally overdispersed, with approximately six neighbours on average (Fig. 1g–i and Extended Data Fig. 2g). In contrast, immature (typically short-lived) colonies were randomly distributed or clumped, as has frequently been reported in field studies of ant and termite populations[20,21,25,26]. These theoretical results correspond well with our analyses of empirical nest distributions for diverse social-insect species from Africa, North and South America, and Australia (Fig. 1, Extended Data Figs 3 and 4 and Supplementary Information section 4.1). Although the degree of hexagonal regularity differs somewhat among sites owing to variable topo-edaphic and floristic uniformity, the repeated emergence of such patterns in diverse contexts worldwide—despite the ubiquity of environmental heterogeneity—affirms the generality of the phenomenon[27].

Our general social-insect model also reproduced the spatial distribution of Namibian FCs[10] (Fig. 1f–i and Extended Data Figs 3 and 4), showing that the large-scale hexagonal pattern of mature circles and the small-scale heterogeneity of immature circles[22,28] can theoretically be explained by termite activity, contrary to recent arguments[17]. However, this finding does not exclude the possibility that SDF concurrently drives vegetation patterning in this arid system. Therefore, we next developed a theoretical framework incorporating simultaneous social-insect and vegetation self-organization and applied it to the Namibian FC system. In the model, termites increase grass mortality on/around nest sites[7,8] and forage on dead biomass in the surrounding matrix. To model vegetation (parameterized as a generic tussock grass, such as the *Stipagrostis* spp. bushman-grasses that dominate much of

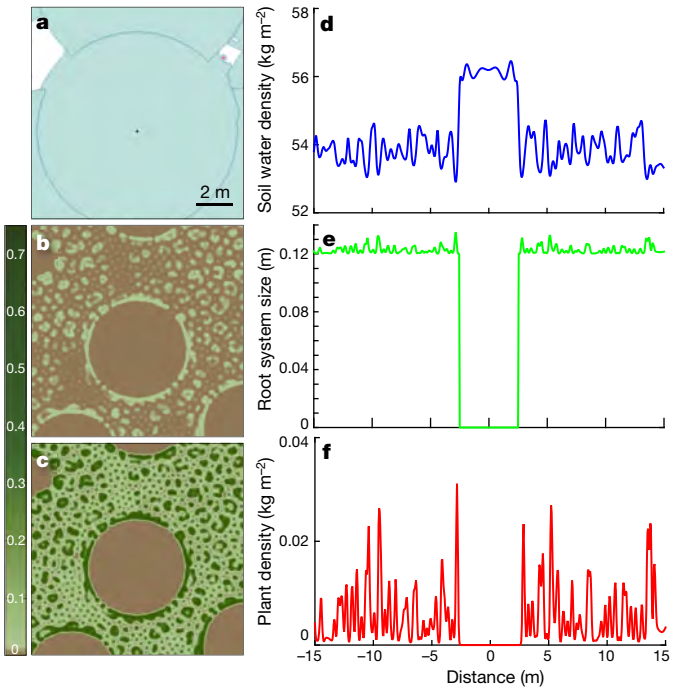

Figure 2 | Simulation of FC emergence from termite engineering and vegetation feedbacks. a, Termite nest (blue dot) with roughly circular foraging territory. **b**, **c**, Characteristic FC vegetation arising around nest site after (**b**) dry and (**c**) wet seasons; brown, soil; green, vegetation; darker green indicates greater biomass according to colour-gradient bar on the left (units are kilograms per square metre). **d**–**f**, Model-predicted soil moisture, root-system size, and plant-density profiles along 30-m transects through simulated FCs (0, nest centre). Parameterization in Extended Data Tables 1 and 2.

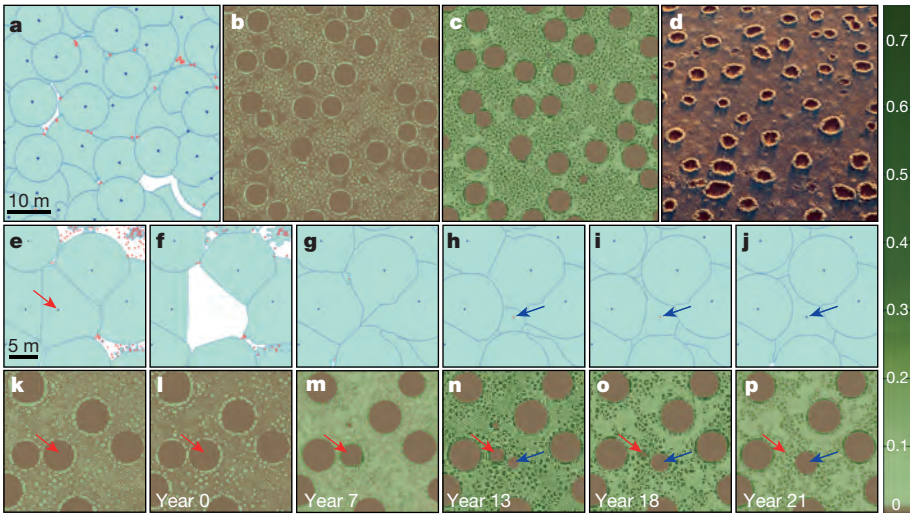

Figure 3 | FC life cycle in the coupled termite-vegetation model. a, Nest centres and foraging territories (blue dots, mature colonies; red dots, incipient nests, including the initial diggings of an alate pair). **b**, **c**, FCs and matrix vegetation following (**b**) dry and (**c**) wet seasons; colour scheme as in Fig. 2b; scale bar as in **a**. **d**, Aerial photograph of FCs at NamibRand Nature Reserve (image courtesy of F. Lanting). **e**–**p**, Termite-colony dynamics (**e**–**j**) and, below each panel, corresponding FC vegetation dynamics (**k**–**p**) for a progression of years in the simulation; scale bar as in **e**. Red arrow in **k**–**p** indicates location of FC shrinkage and disappearance following death of the colony indicated by a red arrow in **e**. Blue arrow in **n**–**p** indicates location of FC appearance and growth following establishment of a new colony (per blue arrow in **h**–**j**). See Supplementary Video 2 for model dynamics. Parameterization in Extended Data Tables 1 and 2.

the Namib Desert), we modified a widely used partial-differential-equation SDF model[15] previously applied to Namibian FCs[9,10] by (1) incorporating stochastic rainfall based on 10-year records from NamibRand Nature Reserve (Extended Data Fig. 5) and (2) allowing for asymmetric root-biomass growth and water uptake in areas with higher moisture concentrations. We parameterized this model using appropriate values from the literature (Extended Data Tables 1, 2).

In this coupled model, termites and vegetation dynamically self-organize and interact. Bare FC discs with elevated soil moisture emerge around nests under arid conditions (Fig. 2 and Extended Data Fig. 6). If rainfall increases, however, plant regeneration outpaces termite-induced mortality, and FCs revegetate (Extended Data Fig. 7), possibly explaining why FCs are absent from *Psammotermes* nests in mesic regions[17] (moisture-mediated plasticity in termite-foraging behaviour has been suggested as another explanation[22]). Asymmetric root-biomass growth and water uptake by plants surrounding the moisture-rich bare discs (Fig. 2d, e) promotes emergence of dense, tall grass rings such as the FC 'perennial belts'[7] (Fig. 2b, c, f), an important feature not predicted by previous SDF models[9,10]. FC life cycles emerge in our model, driven by colony establishment, growth, and death (Fig. 3 and Supplementary Video 2). FCs emerge quickly following colony establishment, but disappear more slowly after colonies die (Fig. 3k–p) as grasses invade and eventually fill the bare patches (Fig. 3 and Extended Data Fig. 6e, f). The weakly bimodal distribution of FC lifespans ranges broadly from <5 to >165 years (Extended Data Fig. 8), with a peak at <15 years and another at about 30–60 years, consistent with the range of existing empirical estimates[6,7,22]. The results above accord with published empirical data and satisfy quantitative criteria proposed to characterize the Namibian FC system[6,7,12,17,22].

Our coupled model also predicts a previously unrecognized feature of these Namib Desert landscapes. Prior studies have focused exclusively on the FCs and have largely ignored the matrix in between. In our model, SDF induces dynamic self-organization of the matrix vegetation, but at smaller spatial scales that are more compatible with ecohydrologically realistic grass–water feedback distances (Supplementary Video 3). Following wet seasons, small, regular clumps of matrix vegetation emerge, interspersed with larger, randomly distributed clumps (Fig. 2c). These larger clumps are rare in the SDF-only model without termites, but arise in the coupled model from small-scale soil-moisture variability in the matrix (Fig. 2d; consistent with published data[22])—itself a ripple effect created by the FCs (Extended Data Fig. 6). To evaluate these theoretical predictions, we photographed NamibRand Nature Reserve matrix-vegetation distributions from 10-m height in February 2015 and characterized both observed and model-predicted patterns using Fourier-transform analyses (see Methods). We found strong agreement between model outputs and field data (Fig. 4).

Thus, by treating vegetation SDF and faunal engineering as complementary processes rather than competing alternatives, our model achieves the most comprehensive and realistic description of this system so far. Whereas previous SDF models can reproduce only the

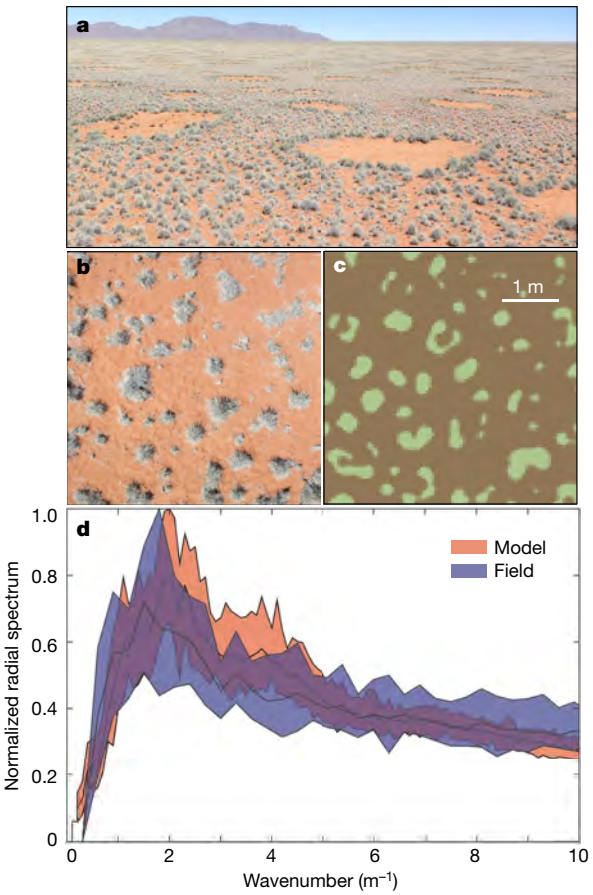

Figure 4 | Predicted and observed regular patterning of FC matrix vegetation. a, Panorama of NamibRand Nature Reserve FC landscape showing matrix-vegetation clumps (photograph by J.A.G.). **b**, Low-altitude (10-m) image of matrix vegetation (photograph by T.C.C.). Scale bar as in **c**. **c**, Model output used for comparison with **b**. Parameterization in Extended Data Tables 1 and 2. **d**, Normalized radial spectra of field images ($n = 27$ samples) and model simulations ($n = 52$ samples), as functions of wavenumber. See dynamics of matrix vegetation in Supplementary Video 3.

formation and qualitative dynamics of hexagonally patterned bare discs[9,10,13], our incorporation of termite self-organization and its feedbacks with SDF yields emergent properties absent from previous models but present in the real landscape, including vegetation size structure and the hitherto undocumented small-scale patterning of matrix vegetation.

Finally, we asked how the interplay of faunal engineering and SDF influenced ecosystem responses to climatic perturbations. Simulated drought (20% reduction in rainfall sustained over 1, 5, or 10 years) reduced system-wide vegetation biomass, but these losses were smaller (that is, landscapes were more drought-resistant) when termites were present. This occurred because the densely vegetated rings and large matrix tussocks generated by the termite–SDF interaction are more drought-resistant and persist after the small matrix patches disappear. Returning rainfall to baseline after drought enabled regeneration of matrix vegetation in systems both with and without termites; however, recovery occurred faster in the coupled termite–SDF system, because the perennial rings and large matrix clumps act as drought refugia and post-drought propagule sources (Supplementary Video 4). Thus, plant–water–consumer feedbacks sustain the productivity of the Namib Desert by enhancing both its resistance to and recovery from climatic perturbations, as hypothesized in recent work[7].

Collectively, our results not only show that interactions among social-insect colonies and vegetation can explain a diverse global suite of regular spatial patterns, but also emphasize the potential for co-occurrence and complementarity among distinct patterning mechanisms in generating multi-scale regularity[4,30]. This highlights the need to focus theoretical and empirical effort on the ways in which multiple mechanisms interact across scales to structure ecosystems[27]. Advances in satellite imaging have buoyed the study of ecological self-organization, but remain insufficient to reveal small-scale patterns. Likewise, evaluating the causes of particular patterns and elucidating multi-mechanism feedbacks will require manipulative field experimentation and ground-based estimation of little-understood phenomena, such as foraging behaviours and competitive dynamics of cryptic ecosystem-engineer species, the ways in which plants and SDF respond to bioturbation and climatic variability and the movement of water through soil in different environmental contexts. Equipped with such knowledge, it may be possible to identify reliable signatures of different mechanisms and to specify the scales at which they act and interact.

Online Content Methods, along with any additional Extended Data display items and Source Data, are available in the online version of the paper; references unique to these sections appear only in the online paper.

Received 20 May; accepted 15 November 2016.

1. Rietkerk, M. & van de Koppel, J. Regular pattern formation in real ecosystems. *Trends Ecol. Evol.* **23,** 169–175 (2008).
2. Scheffer, M. *et al.* Early-warning signals for critical transitions. *Nature* **461,** 53–59 (2009).
3. Pringle, R. M., Doak, D. F., Brody, A. K., Jocqué, R. & Palmer, T. M. Spatial pattern enhances ecosystem functioning in an African savanna. *PLoS Biol.* **8,** e1000377 (2010).
4. Bonachela, J. A. *et al.* Termite mounds can increase the robustness of dryland ecosystems to climatic change. *Science* **347,** 651–655 (2015).
5. Cramer, M. D. & Barger, N. N. Are mima-like mounds the consequence of long-term stability of vegetation spatial patterning? *Palaeogeogr. Palaeoclimatol. Palaeoecol.* **409,** 72–83 (2014).
6. Tschinkel, W. R. The life cycle and life span of Namibian fairy circles. *PLoS ONE* **7,** e38056 (2012).
7. Juergens, N. The biological underpinnings of Namib Desert fairy circles. *Science* **339,** 1618–1621 (2013).
8. Vlieghe, K., Picker, M., Ross-Gillespie, V. & Erni, B. Herbivory by subterranean termite colonies and the development of fairy circles in SW Namibia. *Ecol. Entomol.* **40,** 42–49 (2015).
9. Zelnik, Y. R., Meron, E. & Bel, G. Gradual regime shifts in fairy circles. *Proc. Natl Acad. Sci. USA* **112,** 12327–12331 (2015).
10. Getzin, S. *et al.* Adopting a spatially explicit perspective to study the mysterious fairy circles of Namibia. *Ecography* **38,** 1–11 (2015).
11. Getzin, S. *et al.* Discovery of fairy circles in Australia supports self-organization theory. *Proc. Natl Acad. Sci. USA* **113,** 3551–3556 (2016).
12. Cramer, M. D. & Barger, N. N. Are Namibian "fairy circles" the consequence of self-organizing spatial vegetation patterning? *PLoS ONE* **8,** e70876 (2013).
13. Fernandez-Oto, C., Tlidi, M., Escaff, D. & Clerc, M. G. Strong interaction between plants induces circular barren patches: fairy circles. *Phil. Trans. R. Soc. A* **372,** 20140009 (2014).
14. Meron, E. Modeling dryland landscapes. *Math. Model. Nat. Phenom.* **6,** 163–187 (2011).
15. Gilad, E., von Hardenberg, J., Provenzale, A., Shachak, M. & Meron, E. A mathematical model of plants as ecosystem engineers. *J. Theor. Biol.* **244,** 680–691 (2007).
16. Deblauwe, V., Couteron, P., Lejeune, O., Bogaert, J. & Barbier, N. Environmental modulation of self-organized periodic vegetation patterns in Sudan. *Ecography* **34,** 990–1001 (2011).
17. Getzin, S. *et al.* Clarifying misunderstandings regarding vegetation self-organisation and spatial patterns of fairy circles in Namibia: a response to recent termite hypotheses. *Ecol. Entomol.* **40,** 669–675 (2015).
18. Tschinkel, W. R. Experiments testing the causes of Namibian fairy circles. *PLoS ONE* **10,** e0140099 (2015).
19. Levings, S. C. & Traniello, J. Territoriality, nest dispersion, and community structure in ants. *Psyche (Stuttg.)* **88,** 265–319 (1981).
20. Korb, J. & Linsenmair, K. E. The causes of spatial patterning of mounds of a fungus-cultivating termite: results from nearest-neighbour analysis and ecological studies. *Oecologia* **127,** 324–333 (2001).
21. Grohmann, C., Oldeland, J., Stoyan, D. & Linsenmair, K. E. Multi-scale pattern analysis of a mound-building termite species. *Insectes Soc.* **57,** 477–486 (2010).
22. Juergens, N. *et al.* Weaknesses in the plant competition hypothesis for fairy circle formation and evidence supporting the sand termite hypothesis. *Ecol. Entomol.* **40,** 661–668 (2015).
23. Laurie, H. Optimal transport in central place foraging, with an application to the overdispersion of heuweltjies. *S. Afr. J. Sci.* **98,** 141–146 (2002).
24. Ryti, R. T. & Case, T. J. The role of neighborhood competition in the spacing and diversity of ant communities. *Am. Nat.* **139,** 355–374 (1992).
25. Schuurman, G. & Dangerfield, J. M. Dispersion and abundance of *Macrotermes michaelseni* colonies: a limited role for intraspecific competition. *J. Trop. Ecol.* **13,** 39–49 (1997).
26. Adams, E. S. & Tschinkel, W. R. Spatial dynamics of colony interactions in young populations of the fire ant *Solenopsis invicta*. *Oecologia* **102,** 156–163 (1995).
27. Pringle, R. M. & Tarnita, C. E. Spatial self-organization of ecosystems: integrating multiple mechanisms of regular-pattern formation. *Annu. Rev. Entomol.* **62,** 359–377 (2017).
28. Juergens, N. Exploring common ground for different hypotheses on Namib fairy circles. *Ecography* **38,** 12–14 (2015).
29. Thorne, B. L. & Haverty, M. I. A review of intracolony, intraspecific, and interspecific agonism in termites. *Sociobiology* **19,** 115–145 (1991).
30. Liu, Q.-X. *et al.* Pattern formation at multiple spatial scales drives the resilience of mussel bed ecosystems. *Nature Commun.* **5,** 5234 (2014).

Supplementary Information is available in the online version of the paper.

Acknowledgements This research is a product of US National Science Foundation grant DEB-1355122 to C.E.T. and R.M.P., with seed funding provided by the Princeton Environmental Institute's Grand Challenges Program. J.A.B. was supported by the Marine Alliance for Science and Technology for Scotland (MASTS) pooling initiative, funded by the Scottish Funding Council (HR09011) and contributing institutions. WorldView-2 satellite imagery was obtained through a grant from the DigitalGlobe Foundation to R.A.L. We thank the Government of Namibia, N. Oldendaal and NamibRand Nature Reserve (www.namibrand.org) for permission to conduct research and for providing rainfall data; A. Lamb, D. Doak, E. Lombardi, G. Barrenechea, P. Davies, S. Levin, R. Martinez-Garcia, I. Rodriguez-Iturbe, A. Sabatino, and J. Ware for discussions and assistance; I. Arndt for Australian termite-mound images used in analyses and shown in Extended Data Fig. 3; and F. Lanting for connecting us to NamibRand Nature Reserve and for use of the image in Fig. 3d.

Author Contributions C.E.T., J.A.B., and R.M.P. conceived the study and developed the models, with input from E.S. J.A.B. performed point-pattern analyses and all simulations. E.S. performed Voronoi and Fourier transform analyses. J.A.G., T.C.C., and R.A.L. contributed field data and remote-sensing analyses. C.E.T., J.A.B., and R.M.P. drafted the paper, and all authors provided comments.

Author Information Reprints and permissions information is available at www.nature.com/reprints. The authors declare no competing financial interests. Readers are welcome to comment on the online version of the paper. Correspondence and requests for materials should be addressed to C.E.T. (ctarnita@princeton.edu) or J.A.B. (juan.bonachela@strath.ac.uk).

Reviewer Information *Nature* thanks A. Hastings, N. Juergens, and M. Rietkerk for their contribution to the peer review of this work.

METHODS

No statistical methods were used to predetermine sample size. The experiments were not randomized. The investigators were not blinded to allocation during experiments and outcome assessment.

Termite dynamics. To characterize the emergent spatial organization of termite nests, we developed a general mechanistic model for termite colony growth, reproduction, foraging behaviour, and intraspecific competition (see complete description in the Supplementary Information). For computational convenience, we update these dynamics on a yearly basis. We consider a finite landscape consisting of a regular square lattice. As the initial condition, a single colony founds a nest at a random location within the grid, with a starting population of two termites (queen and king) and a minimum viable foraging area $A_{\min}$. This inaugural colony grows, reproduces, and seeds the rest of the system with new incipient colonies; the system develops with time according to the rules detailed below. Each colony, i, is characterized by its population biomass, $B_i(t)$, and total foraging-territory area, $A_i(t)$.

Foraging territory area. Termites forage outwards from the nest, which is situated at the centre of the initial territory. Thus territories expand in a circular fashion; however, because expansion in certain directions may be blocked by other colonies (see Competition), territory shape does not necessarily remain circular or centred on the nest proper. $R_i(t)$ denotes the largest radial distance within the territory, measured from the centre of the nest; this radius is constrained physiologically by $R_{\max}$, the maximum distance that a foraging termite can travel.

Nest. We assume that the physical nest proper occupies a circular area, $M_i(t)$ (centred within the initial territory), whose radius is a fraction of $R_i(t)$ given by f_m.

Colony growth. We model colony size and growth in terms of biomass and, consistent with empirical data[31], we assume that termite colonies grow logistically. Production of new colony members, μ, is determined by the queen's constant rate of egg-laying. The carrying capacity, $B_{\max}$, represents the maximum possible biomass that a colony can reach, a limit that we assume to be imposed by intrinsic physiological constraints (for example, how big a nest structure the colony can construct) and thus equivalent for all colonies. Colony members die at a per capita mortality rate m. The effective carrying capacity is therefore $B_{\max}(1-m/\mu)$. To meet basic energetic maintenance costs and achieve growth, colonies require resources. Specifically, the resources needed to maintain colony i at size $B_i(t)$ are given by $\rho_i^{\text{need}} = B_i(t)/c$, where c is the termite assimilation capacity (that is, the conversion factor from resource biomass into termite biomass). This resource requirement is to be compared with the resources available in the foraging territory. Since we model termites that feed exclusively on dead plant material, we assume that resource availability for colony i at time t at any given location x within that colony's territory is equal to the amount of dead plant material that has accumulated at that location during the previous year. Assuming that plant mortality occurs at a constant rate, m_P, and given that colony i occupies area $A_i(t)$ at time t, the resources available to colony i, $\rho_i(t)$, are

$$\rho_i(t) = \int_{A_i(t)} \int_{1\text{year}} m_P P(\boldsymbol{x}, t')\mathrm{d}t'\mathrm{d}\boldsymbol{x}$$

where $P(\boldsymbol{x}, t)$ is the live plant biomass at location $\boldsymbol{x}$ and time t. This will be obtained from the dynamics of the vegetation model below. Because termite dynamics are updated annually, resource requirement and availability are compared at the beginning of each year. If $\rho_i \neq \rho_i^{\text{need}}$, the colony will try to adjust its foraging territory accordingly: if resources are insufficient ($\rho_i < \rho_i^{\text{need}}$), the colony will expand its foraging territory trying to obtain the necessary resources; conversely, if resources are in excess ($\rho_i > \rho_i^{\text{need}}$), termites will not need to travel as far to harvest the minimum necessary resources, and the foraging territory will shrink. Such shrinkage produces 'empty' (unoccupied) area potentially available for nearby colonies as additional foraging territory. If territory expansion is hindered for any reason (for example, lack of available space, or $R_{\max}$ being reached), then colony biomass will grow only as much as allowed by the resources available up to the point of hindrance.

Territorial competition. If territory expansion leads to overlap with the territory of another colony, we assume that a conflict ensues at the border between the two territories in the form of direct interference competition, avoidance, and/or aggressive territorial defence (such antagonism between intraspecific colonies is common among many, perhaps most, species of termites and ants[29,32]). These conflicts can simply remain as border skirmishes (that is, offsetting mortalities, neither colony gains any net ground) or can lead to 'wars' that may result in the extermination of one colony. We assume that smaller, growing colonies exhibit more aggressively expansionist tendencies than do larger established ones, in keeping with evidence that aggression declines with distance from the nest[33] (Supplementary Fig. 1a). The outcome is probabilistic, with $P(i \text{ and } j \text{ at war}) = P(i \text{ seeks war}) \times P(j \text{ seeks war})$, where

$$P(i \text{ seeks war}) = \frac{1}{1+\mathrm{e}^{-\beta_2(1-\alpha_2 S_i(t))}}, \quad \text{with} \quad S_i(t) = \frac{B_i(t)}{B_{\max}}$$

where α_2 is a reference value and β_2 is a shape factor for the probability of engaging in conflict. War results either in the death of one colony (highly probable if there is a substantial size discrepancy since we assume ~1:1 mortality in conflict) or in coexistence (if sizes are similar), in which case the workers' foraging radius is truncated, a boundary is established, and expansion ceases in that direction. If colonies i and j fight, then i wins with probability

$$P(i \text{ beats } j) = \frac{1}{1+\mathrm{e}^{-\beta(1-\alpha S_j(t)/S_i(t))}}$$

where α is a reference value and β is a shape factor for the conflict outcome probability. If colony i dies in conflict, the winning colony j also suffers losses in the form of reductions in both territory and population biomass: $A_j' = A_j - A_i$, and B_j is reduced proportionally (that is, $B_j' = B_j\,(A_j'/A_j)$). In the rare event that the winning colony has a smaller territory and biomass than the losing one, then both territory and population biomass are decreased to a fraction q of the original: $A_j' = qA_j$. In either case, the winning area cannot be reduced below the minimum, $A_{\min}$.

Reproduction. We assume that when colonies reach a certain population biomass, $B_{\text{mat}} < B_{\max}$, they become reproductively mature (also known as established) and produce alates (winged dispersing future queens and kings) as follows. If, during the current time step, colony i shrinks in biomass owing to resource limitation, then it forgoes reproduction even if its newly reduced biomass exceeds B_{mat}; otherwise, it produces a number of alates proportional to a fraction f_A of its biomass. In our simulations we assume that these alates disperse randomly and in pairs over the entire grid. If an alate pair lands within the territory of an established colony or does not have enough space to initiate (that is, available area at the landing point $< A_{\min}$), the alates die. Otherwise, they start a new colony. The landing point is assumed to be the centre of the new nest.

Mortality. There are two sources of mortality for colonies. The first is conflict between neighbours (see above), which we assume to be the primary cause of death in small colonies, but to decline in importance as colonies grow. Indeed, empirical observations from multiple systems suggest that territorial conflict eliminates many incipient colonies but seldom leads to the death of a mature colony, whereas mature colonies show signs of perpetual conflict at outer edges of their foraging territories[34–36]. The second source of mortality is an intrinsic stochastic death rate, which primarily affects established colonies. We let m_C be stochastic mortality for large colonies and set it to replicate a realistic lifetime for mature colonies[31,37].

Termite engineering. Here, we focus on the scenario in which termites locally deplete plant biomass, as hypothesized for the sand termite *P. allocerus* (Rhinotermitidae), which has been suggested as the cause of the Namibian FCs[7]. On nests, we assume the mortality rate of plant biomass to be elevated by a fixed proportion ν: $m_{P\text{off}} = m_P$; $m_{P\text{on}} = \nu m_{P\text{off}}$. For full model details and analysis see Supplementary Information; for parameterization see Extended Data Table 1.

Vegetation dynamics. To model vegetation dynamics, we modified a model that has been used repeatedly to describe and reproduce the patterns that are typical of vegetation in semi-arid environments[15]. The model considers the dynamics of vegetation (P), soil water (W), and surface water (O) densities. Assuming a flat terrain, the model can be written as

$$\frac{\partial P(\boldsymbol{x},t)}{\partial t} = G_P(\boldsymbol{x},t)P(\boldsymbol{x},t)\left(1-\frac{P(\boldsymbol{x},t)}{K}\right) - m_P P(\boldsymbol{x},t) + D_P\nabla^2 P(\boldsymbol{x},t) \quad (1)$$

$$\frac{\partial W(\boldsymbol{x},t)}{\partial t} = \gamma\frac{P(\boldsymbol{x},t)+QW_0}{P(\boldsymbol{x},t)+Q}O(\boldsymbol{x},t) - N\left(1-\frac{R_{\text{educ}}P(\boldsymbol{x},t)}{K}\right)W(\boldsymbol{x},t) - G_W(\boldsymbol{x},t)W(\boldsymbol{x},t) + D_W\nabla^2 W(\boldsymbol{x},t) \quad (2)$$

$$\frac{\partial O(\boldsymbol{x},t)}{\partial t} = R_{\text{ainfall}} - \gamma\frac{P(\boldsymbol{x},t)+QW_0}{P(\boldsymbol{x},t)+Q}O(\boldsymbol{x},t) + D_O\nabla^2(O^2(\boldsymbol{x},t)) \quad (3)$$

where ∇^2 represents the nabla operator (second spatial derivative) and the values and meaning of parameters can be found in Extended Data Table 2. The first term in equation (3) represents rainfall, the second term represents infiltration of surface water into the soil, and the third term represents surface water diffusion. The first term in equation (2) represents the increase in soil water owing to infiltration, whereas the second term represents evaporation, the third term represents soil water uptake, and the last term soil water diffusion. Lastly, the first term in equation (1) represents plant growth due to water uptake, the second term represents mortality, and the third term vegetation biomass diffusion (via, for example, seed dispersal). In turn, G_P and G_W, plant growth rate and soil water consumption rate,

respectively, depend on the extension of the root system. Thus, if the root system is encoded in the kernel:

$$G(\boldsymbol{x},\boldsymbol{x}',t)=\frac{1}{2\pi S_0^2}\exp\left[-\frac{|\boldsymbol{x}-\boldsymbol{x}'|^2}{2[S_0(1+EP(\boldsymbol{x},t))]^2}\right] \quad (4)$$

the effect of roots on growth and water consumption, respectively, is given by

$$G_{\mathrm{P}}(\boldsymbol{x},t)=\Lambda\int_L G(\boldsymbol{x},\boldsymbol{x}',t)\,W(\boldsymbol{x}',t)\mathrm{d}\boldsymbol{x}'$$

$$G_{\mathrm{W}}(\boldsymbol{x},t)=\Gamma\int_L G(\boldsymbol{x}',\boldsymbol{x},t)P(\boldsymbol{x}',t)\mathrm{d}\boldsymbol{x}'$$

where the integrals consider the totality of the system[38]. The kernel determines to what extent roots from a body of vegetation biomass (for example, clump) can use water and influence other parts of the system. Specifically, the Gaussian kernel above sets this distance through its standard deviation, the root-system size, given by $S_0(1+EP(\boldsymbol{x},t))$.

Variable rainfall. We used data to replace the constant average rainfall (typically used in models such as the one above) by a more realistic variable rainfall function $R_{\mathrm{ainfall}}(t)$ that captures the typical Namib Desert yearly rainfall. To that end, we used data from 2004 to 2014 from multiple Namib Desert locations (provided by V. Hartung) to calculate mean monthly rainfall in an 'average' year along with standard errors reflecting among-year variation in monthly totals. The resulting $R_{\mathrm{ainfall}}(t)$ depicts the two distinct seasons (wet and dry) characteristic of this region (see Extended Data Fig. 5):

$$R_{\mathrm{ainfall}}(t)=R_0 10^{\omega\sin\left(\frac{(t+1)\pi}{6}\right)}[1+\sigma_R\eta(t)] \quad (5)$$

Here, t is the month of the year, and the second term in brackets represents noise (random number uniformly distributed between 0 and σ_R) that takes into account an additional source of stochasticity inherently associated with the weather.

Asymmetric roots. One important feature of the vegetation model above is that the root system represented by the Gaussian kernel, equation (4), is symmetric and therefore root density is equivalent in all directions, regardless of heterogeneities in water availability. However, desert-plant roots in sandy substrates both (1) grow preferentially in the direction of localized moisture concentrations (hydrotropism) and (2) exhibit enhanced proliferation, branching, and biomass growth in moist versus dry soil, breaking the symmetry of root architecture in ways thought to enable 'precise exploitation of water patches and drought avoidance'[39]. We therefore modified the above model to incorporate the possibility of hydrotropism and asymmetric root proliferation (or asymmetric exploitation of soil moisture) in response to localized differences in soil-water availability. Once the soil-moisture difference dissipates, the root system in that direction returns to its original growth pattern. We introduced an additional term in the plant-growth equation, equation (1), that modifies plant growth rate by a specific factor. This is calculated by adding to the existing term, $G_{\mathrm{P}}(\boldsymbol{x},t)$, an additional contribution from any direction in which soil water surpasses a site-specific threshold, W_{thr}: $\widetilde{G}_P(\boldsymbol{x},t)=G_{\mathrm{P}}(\boldsymbol{x},t)[1+\omega' F_{\mathrm{asym}}(\boldsymbol{x},t)]$, where ω' is a (dimensionless) diminishing factor (in our simulations, $\omega'=0.5$) that is necessary to prevent numerical instabilities leading to unrealistic features such as system-wide plant clusters, and F_{asym} is the improvement function per se, given by

$$F_{\mathrm{asym}}(\boldsymbol{x},t)=\left\langle\frac{W(\boldsymbol{x}',t)}{W(\boldsymbol{x},t)}\right\rangle_{\boldsymbol{x}'} \quad (6)$$

The $\langle\ldots\rangle$ notation represents spatial averages as follows: following equation (4), the standard deviation of the Gaussian root system is given by $S_0(1+EP(\boldsymbol{x},t))$; therefore, a rough estimate of the maximum length of the root system is given by three times that standard deviation. Thus, the spatial averages in equation (6) consider locations at a distance $|\boldsymbol{x}-\boldsymbol{x}'|\approx 3S_0(1+EP(\boldsymbol{x},t))$and use the immediate neighbourhood of these locations to assess the average water availability and how different it is from $W(\boldsymbol{x},t)$. Because our simulations occur on a square lattice, such spatial average only considers the four neighbours of a location $\boldsymbol{x}'$. However, only nearest neighbours of $\boldsymbol{x}'$ fulfilling

$$\frac{W(\boldsymbol{x}'_{nn},t)}{W(\boldsymbol{x},t)}-W_{\mathrm{thr}}>0$$

are considered for the average, which ensures that only a sufficiently large contrast between the focal location x and the neighbourhood of $\boldsymbol{x}'$ triggers this differential root growth. In our simulations, we set $W_{\mathrm{thr}}=4$.

Parameterization and sensitivity analysis. We thoroughly searched the existing literature to identify plausible (and internally consistent) values of individual-, colony-, and population-level parameters such as termite individual biomass, thresholds for maturity and reproduction, and the parameters related to the vegetation model (Extended Data Tables 1 and 2). For the parameters related to the vegetation model, we modified previous parameterizations[15] to tailor the model to Namib Desert conditions (for example, the variable rainfall function described above, low surface-water diffusivity). In addition, we conducted sensitivity analyses to test the dependence of the model outputs on each of the different parameters. Finally, because we used a spatial discretization to enhance the speed of our simulations, we conducted additional sensitivity analyses to test the appropriateness of (1) the spatial grain and (2) topology (square versus hexagonal lattice) of the underlying grid, showing that these assumptions did not affect the results.

Insect-nest distributions: field data. We used high-resolution satellite imagery to quantitatively analyse the spatial distribution of social-insect nests in four countries on three continents: termite mounds in Kenya (Macrotermitinae: *O. montanus*; Fig. 1b), Mozambique (Macrotermitinae: *Macrotermes* spp.; Fig. 1e), Brazil (Termitidae: *S. dirus*; Fig. 1c), and Australia (Termitidae: *Amitermes meridionalis*), along with harvester ant nests in the southwestern USA (Formicidae: *Pogonomyrmex* spp.; Fig. 1d). In all cases, these features were clearly distinguishable in imagery (Fig. 1 and Extended Data Fig. 3) and the identities of the insect species that built them have been unambiguously established in published field studies (Supplementary Information section 4.1). We further re-analysed the Namibian FC sites of a previous study[10] to ensure concordance and comparability with our other analyses. The regions and locations analysed are as follows:

Kenya. Two topographically, edaphically, and floristically homogeneous rectangular areas (0.975 km^2 and 1.201 km^2, comprising 205 and 241 mounds, respectively) in clay-rich vertisols at Mpala Research Centre (~0° 17′ N, 36° 51′ E), where our previous work has extensively ground-truthed mound locations[3], from high-resolution multispectral Pleiades-1 satellite imagery from May 2013.

Mozambique. A subsection of a 0.630-km^2 rectangular area of mixed *Acacia*/palm savanna-woodland in Gorongosa National Park (~18° 57′ S, 34° 21′ E) comprising ~152 total mounds, from high-resolution multispectral WorldView-2 satellite imagery supplied by the DigitalGlobe Foundation; this analysis was comprehensively ground-truthed by mapping all mounds on foot.

Brazil. Two areas (0.209 and 0.409 km^2, comprising ~452 and 751 mounds, respectively), in Bahia State (~12° 30′ S, 41° 37′ W), from Google Earth (image copyright 2016, CNES/Astrium).

North America. Two areas of 0.308 and 0.179 km^2, comprising ~510 and 224 nests, respectively, in Arizona (~36° 15′ N, 113° 05′ W), from Google Earth (image copyright 2012, DigitalGlobe).

Australia. Two oblique aerial photographs (courtesy of photographer I. Arndt) of *Amitermes* mounds in Litchfield National Park, comprising 249 and 295 mounds, respectively. Specific geographic coordinates for these images are unknown, and we were unable to analyse these mounds in satellite images; generic coordinates for Litchfield are ~13° 17′ S, 130° 45′ E.

Namibia. Three Namib-Desert sites within the Giribes Plain (G) and Marienfluss Valley (MV), within the same rectangular areas analysed in previous work[10], with areal extents of 0.288 (G1), 0.294 (G2), and 0.322 km^2 (MV), and comprising 1,181, 1,288 and 676 FCs, respectively, from Google Earth (image copyright 2016, DigitalGlobe).

Insect-nest distributions: quantitative analysis. We analysed the spatial distribution of termite mounds, ant nests, and FCs (henceforth, 'points'). We computed Voronoi tessellations[10,40] for the point patterns, from which we extracted the following information: (1) distributions of nearest-neighbour numbers for each point, that is, the number of corners of each Voronoi tile, which provides information on the regularity of the pattern (Fig. 1g and Extended Data Fig. 3); (2) distributions of tile areas (mean area and coefficient of variation); and (3) distributions of the distances of all points to their nearest neighbour[10]. Following ref. 10, for these analyses we removed all edge tiles with corners touching the borders of the analysed area. Therefore, the effective number of nests analysed for each area was smaller than the total number of nests present. We further calculated pairwise correlation and Ripley's L functions[41] for each different area (see Supplementary Information and Extended Data Fig. 4). We used both the 'spatstat' package[41] in R and our own Fortran code to calculate both functions. We also used 'spatstat' to calculate significance envelopes. We used the same approach to analyse the output of the theoretical model (Fig. 1g and Extended Data Figs 2–4).

Vegetation patterns: field data. We collected low-altitude aerial imagery of Namibian FC and matrix vegetation at the NamibRand Nature Reserve in southern Namibia (25.04° E, 15.94° S), where FCs have been intensively studied and biotic/abiotic conditions are well characterized[6,7,12]. Mean annual precipitation is 70–80 mm (ref. 6), falling mostly from December to May. The site consists of

Kalahari sand plains and dunes typical of the habitat in which FCs are found[6,7,12]. The flora is co-dominated by three congeneric bushman-grasses: *Stipagrostis obtusa*, *Stipagrostis uniplumis*, and *Stipagrostis ciliata*[12]. In February 2015, we selected ten sites spanning ~35 km within NamibRand Nature Reserve. At each site, we haphazardly selected ten pairs of FCs and measured the distance between circles (from one outer ring edge to another) and the size of each FC (average of two perpendicular diameters within the vegetation ring). The mean (±s.e.m.) diameter of FCs in our data set was 5.94 ± 0.23 m, and the mean distance between circles was 6.9 ± 0.4 m. Low-altitude imagery was collected at a subset of three sites: the most northern (24.94° E, 25.95° S), the most southern (25.25° E, 16.02° S), and the most central (25.13° E, 16.01° S). We photographed matrix vegetation at the midpoint between 30 pairs of neighbouring FCs ($n = 10$ pairs per site; Fig. 4b) using a digital camera (Canon PowerShot S110), mounted on an 11-m carbon-fibre pole (Ron Thompson Gangster Carp Pole) such that it could be held parallel to the ground at 10-m height. Before imaging, we manually removed fallen leaf litter that might have obscured spatial patterns in standing vegetation. Exposure was controlled manually to maintain consistency in changing light conditions. For all images, this camera rig was held at constant height by the same individual (T.C.C.). A reference object was placed in all images and used to scale them to a pixel size of 0.333 cm.

Vegetation patterns: quantitative analysis. Images were scaled and a large rectangular sub-area of similar size (1,340 pixels × 1,340 pixels for two sites, and 900 pixels × 900 pixels for a site in which FC density was higher) was selected from each image to comprise only grass and soil (that is, no FCs) and no visible disturbance ($n = 27$ images; three of the images were excluded because they did not have a large enough area between circles). Images were processed as in ref. 4. For comparison with the model simulations with stochastic seasonal rainfall, we selected snapshots of the simulated vegetation in the wet season in different years (we used snapshots from February, corresponding to when the field images were collected in 2015). From these snapshots, we selected 2 subsections (73 pixels × 73 pixels and 135 pixels × 135 pixels) between neighbouring FCs ($n = 52$, 26 years × 2 subsections per year). We used the two-dimensional Fourier transform and a subsequent computation of the two-dimensional periodogram (that is, power spectrum[42]), to provide a quantitative characterization of the spatial patterns[43]. For this analysis, we transformed the patterns of biomass density from the model into binary images (vegetation versus bare soil; see Fig. 4c) according to a threshold that allowed us to eliminate background noise: we selected the threshold to be the highest value for which the Fourier transform analysis does not show any threshold dependence (0.015 kg/m^2). On the basis of the two-dimensional periodogram, we then calculated the radial spectrum $\boldsymbol{r}$ (sum of the periodogram values on concentric ring-shaped regions of the two-dimensional surface), to quantify the portion of image variances that could be accounted for by a simple cosine wave repeating itself r times (wavenumber) along a travel direction of the periodogram. We normalized the radial spectra for (1) wavenumber, by dividing $\boldsymbol{r}$ by the size of the domain in the analysed image (approximately 4.45 and 3 m for field images and 3.65–6.75 m for simulations); and (2) amplitude of the radial spectrum, by dividing by the maximum of the mean.

Data availability statement. The data sets generated and analysed during the current study are available in the Dryad repository at http://dx.doi.org/10.5061/dryad.3264f. The computer code is available from the corresponding authors upon request.

31. Collins, N. M. Populations, age structure and survivorship of colonies of *Macrotermes bellicosus* (Isoptera: Macrotermitinae). *J. Anim. Ecol.* **50,** 293–311 (1981).
32. Holldobler, B. Territoriality in ants. *Proc. Am. Phil. Soc.* **123,** 211–218 (1979).
33. Adams, E. S. Territory size and shape in fire ants: a model based on neighborhood interactions. *Ecology* **79,** 1125–1134 (1998).
34. Darlington, J. P. The underground passages and storage pits used in foraging by a nest of the termite *Macrotermes michaelseni* in Kajiado, Kenya. *J. Zool.* **198,** 237–247 (1982).
35. Palmer, T. M. Wars of attrition: colony size determines competitive outcomes in a guild of African acacia ants. *Anim. Behav.* **68,** 993–1004 (2004).
36. Abe, T., Bignell, D. E. & Higashi, M. *Termites: Evolution, Sociality, Symbioses, Ecology* (Springer, 2000).
37. Keller, L. Queen lifespan and colony characteristics in ants and termites. *Insectes Soc.* **45,** 235–246 (1998).
38. Gilad, E. & von Hardenberg, J. A fast algorithm for convolution integrals with space and time variant kernels. *J. Comput. Phys.* **216,** 326–336 (2006).
39. Guevara, A. & Giordano, C. V. Hydrotropism in lateral but not in pivotal roots of desert plant species under simulated natural conditions. *Plant Soil* **389,** 257–272 (2015).
40. Illian, J., Penttinen, A., Stoyan, H. & Stoyan, D. *Statistical Analysis and Modelling of Spatial Point Patterns* (John Wiley, 2008).
41. Baddeley, A., Rubak, E. & Turner, R. *Spatial Point Patterns: Methodology and Applications with R* (Chapman and Hall/CRC, 2015).
42. Mugglestone, M. A. & Renshaw, E. Detection of geological lineation on aerial photographs using two-dimensional spectral analysis. *Comput. Geosci.* **24,** 771–784 (1998).
43. Couteron, P. & Lejeune, O. Periodic spotted patterns in semi-arid vegetation explained by a propagation-inhibition model. *J. Ecol.* **89,** 616–628 (2001).
44. Tschinkel, W. R. The foraging tunnel system of the Namibian desert termite, *Baucaliotermes hainesi*. *J. Insect Sci.* **10,** 65 (2010).
45. Baker, P. B. & Haverty, M. I. Foraging populations and distances of the desert subterranean termite, *Heterotermes aureus* (Isoptera: Rhinotermitidae), associated with structures in southern Arizona. *J. Econ. Entomol.* **100,** 1381–1390 (2007).
46. Jones, S. C. Colony size of the desert subterranean termite *Heterotermes aureus* (Isoptera: Rhinotermitidae). *Southwest. Nat.* **35,** 285–291 (1990).
47. Haagsma, K. A. & Rust, M. K. Colony size estimates, foraging trends, and physiological characteristics of the western subterranean termite (Isoptera: Rhinotermitidae). *Environ. Entomol.* **24,** 1520–1528 (1995).
48. Grace, J. K., Abdallay, A. & Farr, K. R. Eastern subterranean termite (Isoptera: Rhinotermitidae) foraging territories and populations in Toronto. *Can. Entomol.* **121,** 551–556 (1989).
49. Husseneder, C., Powell, J. E., Grace, J. K., Vargo, E. L. & Matsuura, K. Worker size in the formosan subterranean termite in relation to colony breeding structure as inferred from molecular markers. *Environ. Entomol.* **37,** 400–408 (2008).
50. Wood, T. G. & Sands, W. A. in *Production Ecology of Ants and Termites* (ed. Brian, M. V.) 245–292 (Cambridge Univ. Press, 1978).
51. Matsuura, K. Colony-level stabilization of soldier head width for head-plug defense in the termite *Reticulitermes speratus* (Isoptera: Rhinotermitidae). *Behav. Ecol. Sociobiol.* **51,** 172–179 (2002).
52. Darlington, J. P. E. C. Turnover in the populations within mature nests of the termite *Macrotermes michaelseni* in Kenya. *Insectes Soc.* **38,** 251–262 (1991).
53. Hadley, N. F. & Szarek, S. R. Productivity of desert ecosystems. *Bioscience* **31,** 747–753 (1981).
54. Thorne, B. L., Breisch, N. L. & Muscedere, M. L. Evolution of eusociality and the soldier caste in termites: influence of intraspecific competition and accelerated inheritance. *Proc. Natl Acad. Sci. USA* **100,** 12808–12813 (2003).
55. Golodets, C. *et al.* Climate change scenarios of herbaceous production along an aridity gradient: vulnerability increases with aridity. *Oecologia* **177,** 971–979 (2015).
56. Cain, M. L. & Damman, H. Clonal growth and ramet performance in the woodland herb, *Asarum canadense*. *J. Ecol.* **85,** 883–897 (1997).
57. Milton, S. J. & Dean, W. Disturbance, drought and dynamics of desert dune grassland, South Africa. *Plant Ecol.* **150,** 37–51 (2000).
58. Evangelides, C., Arampatzis, G. & Tzimopoulos, C. Estimation of soil moisture profile and diffusivity using simple laboratory procedures. *Soil Sci.* **175,** 118–127 (2010).
59. Danin, A. *Plants of Desert Dunes* (Springer, 2012).
60. Sheffer, E., Yizhaq, H., Shachak, M. & Meron, E. Mechanisms of vegetation-ring formation in water-limited systems. *J. Theor. Biol.* **273,** 138–146 (2011).

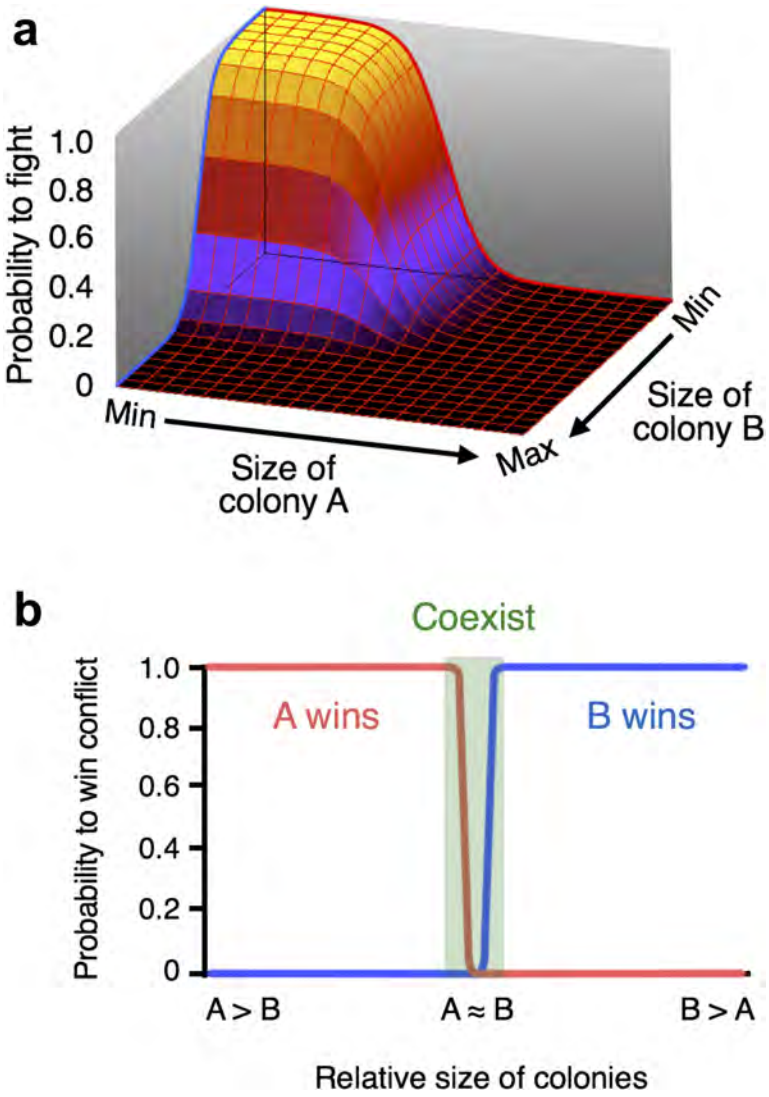

Extended Data Figure 1 | Probability functions associated with conflicts in the termite model. a, Probability for colony *A* and colony *B* to engage in a war as a function of each colony's population biomass. **b**, If colonies *A* and *B* engage in a war, probability functions for colony *A* (red curve) or *B* (blue curve) to win the war as a function of the ratio of colony population biomass. When the two colonies have roughly the same biomass, they coexist (green area).

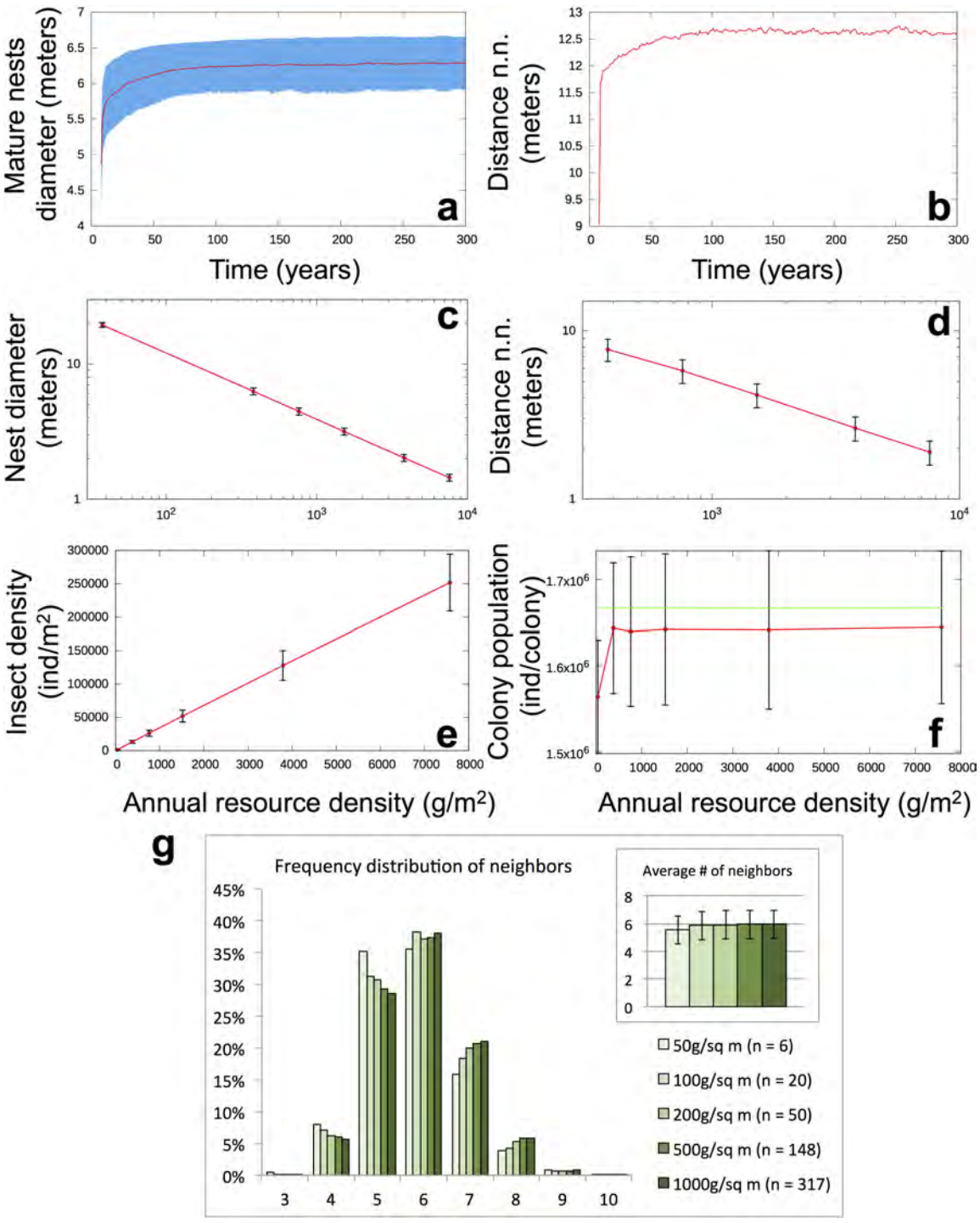

Extended Data Figure 2 | Results of the termite self-organization model with a fixed resource density level, P_{cst}. **a**, **b**, Temporal behaviour of mature colonies in the termite model for $P_{cst} = 50\,g\,m^{-2}$. **a**, Average diameter of mature nests (blue shading, ±1 s.d.). **b**, Average distance between nearest neighbours, (where neighbours are nests that share territory borders). Both observables reach a clear stationary state after a transient period of ~200 years. **c**–**f**, Emergent behaviour for the colonies at the stationary state as a function of the (annually) available level of resources. **c**, Average mound diameter, which reflects foraging-territory area, decreases as resource availability increases. **d**, Mean nearest-neighbour distance also decreases with increasing resource density. **e**, Termite population density (number of individuals per square metre) increases with available resources. **f**, Average colony biomass density (individuals/colony) increases with available resource density, and reaches a saturation value around $B_{max}(1-m/\mu)$ (see Supplementary Information). **g**, Frequency distribution of neighbour numbers from Voronoi analysis for the model with different resource densities (inset: mean number of neighbours). Higher resource densities result in a higher number of colonies (numbers in parentheses in the legend) and therefore more powerful results. Results are obtained by averaging over 100 simulations for each resource level; error bars, ±1 s.d.

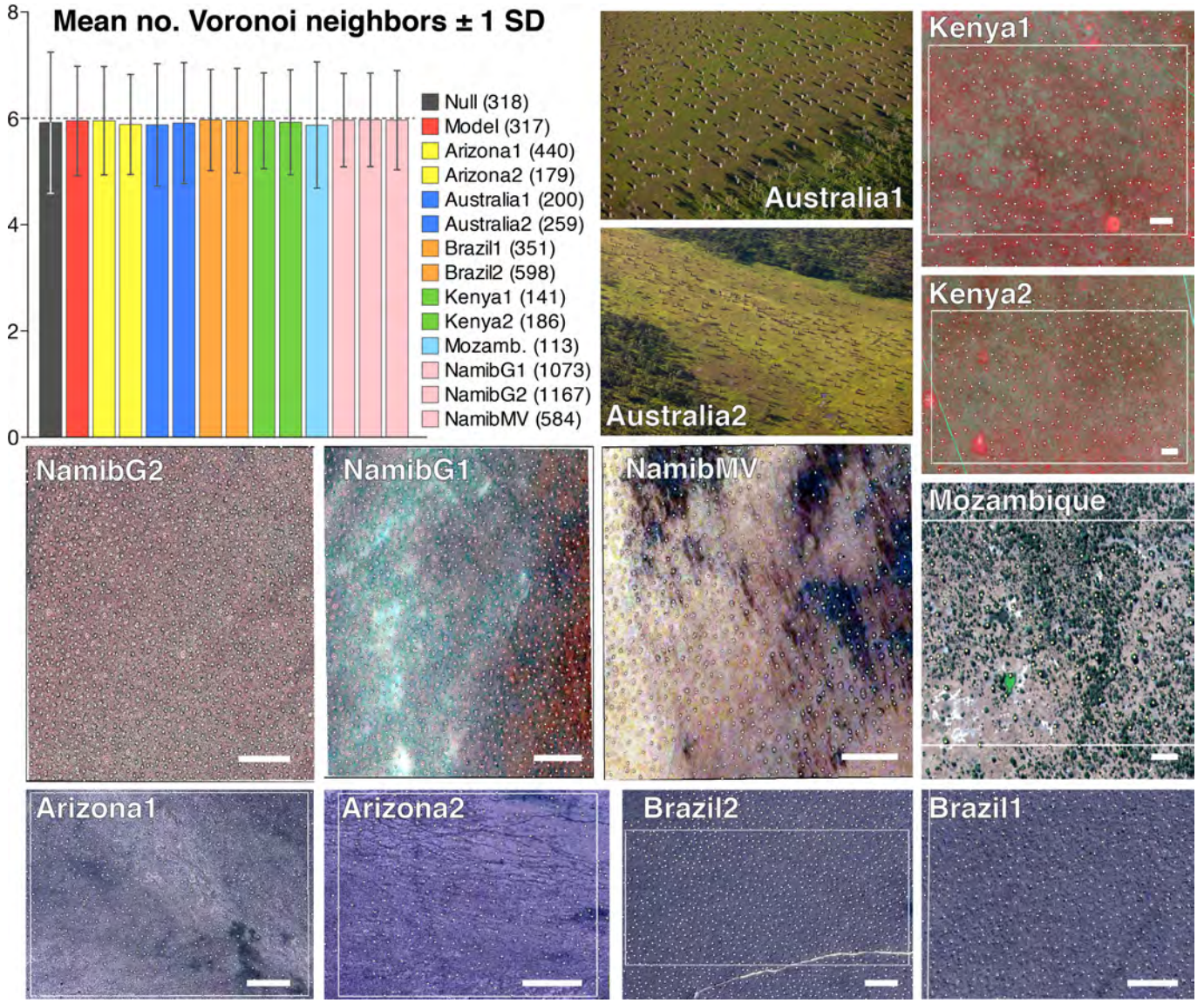

Extended Data Figure 3 | Average number of neighbours in various field locations. Upper left panel: average number of neighbours (±1 s.d.) from Voronoi analysis of model and field data; number of nests at each location is shown in parentheses. All other panels: satellite imagery and/or photographs used for data analysis. Mounds are highlighted for ease of observation. If a white rectangle is present then only the points within the rectangle were analysed; otherwise, the whole image was analysed. All scale bars, 100 m. Aerial photographs of *Amitermes* mounds in Australia courtesy of I. Arndt. Pleiades-1 satellite imagery of Kenya copyright 2013 CNES/Astrium (GeoTIFF file supplied by Apollo Mapping, Boulder, Colorado, USA). Multispectral WorldView-2 satellite imagery of Mozambique courtesy of the DigitalGlobe Foundation. Google Earth satellite imagery: images for Arizona copyright 2012 DigitalGlobe, for Brazil copyright 2016 CNES/Astrium, and for Namibia copyright 2016 DigitalGlobe.

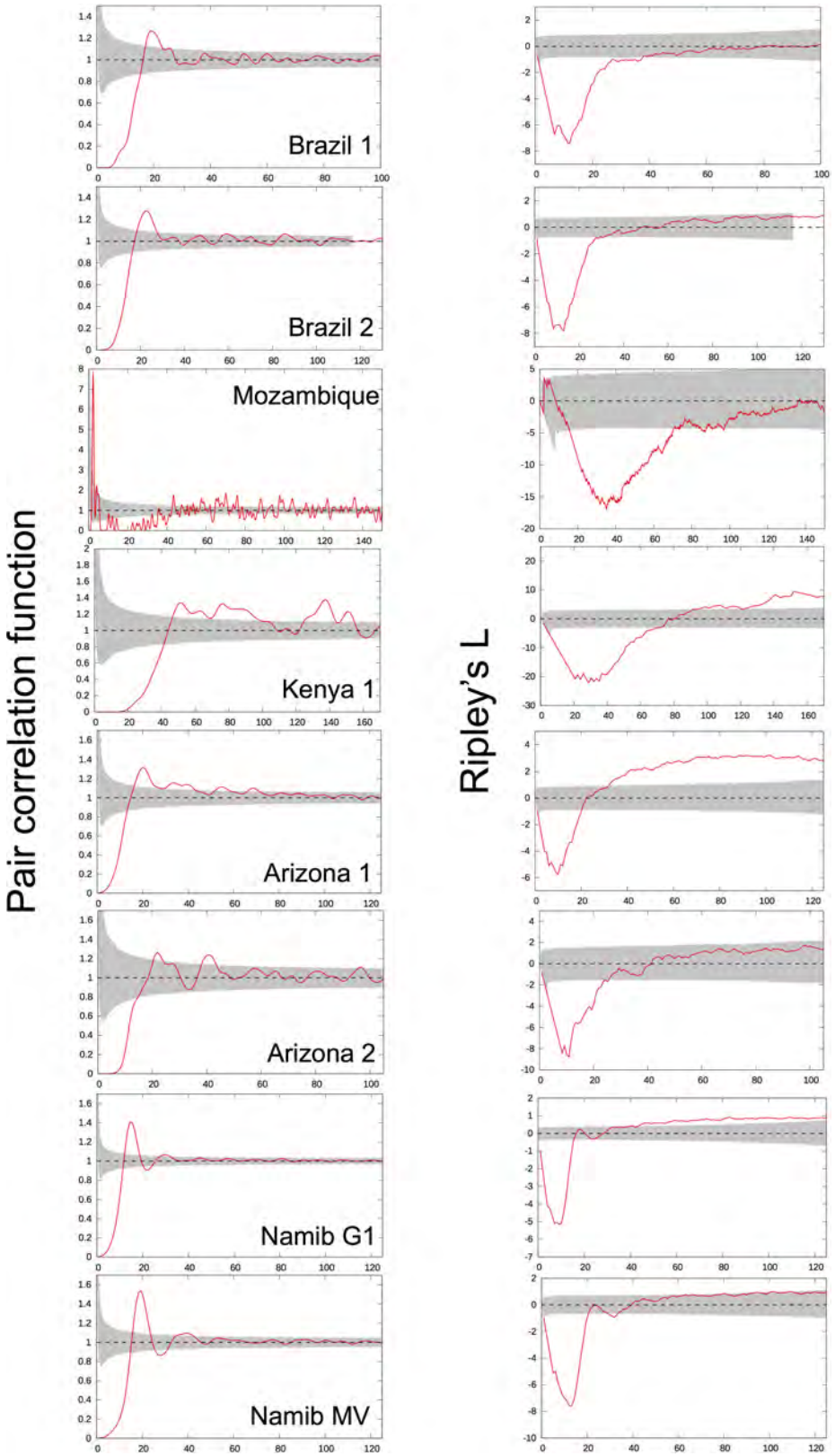

Extended Data Figure 4 | Spatial point-pattern analyses of various field locations. Left: pair correlation function as a function of distances between nests. Right: Ripley's *L* function for the same examples. Ninety-five per cent pointwise simulation envelopes (shaded areas) were calculated using the default function from the R package spatstat. These envelopes allow us to reject the null hypothesis (complete spatial randomness) at a confidence level of 95%; thus, if the focal function (red line) falls out of the envelope for a given distance *r*, the function differs from the expectation for a completely random point distribution. Both sets of panels show peaks (left panels) or valleys (right panels) of regularity that indicate the presence of overdispersion for each of these examples. Note the different number of nests present in the samples from each location (Extended Data Fig. 3), which leads to different levels of noise in the calculation of the two statistics.

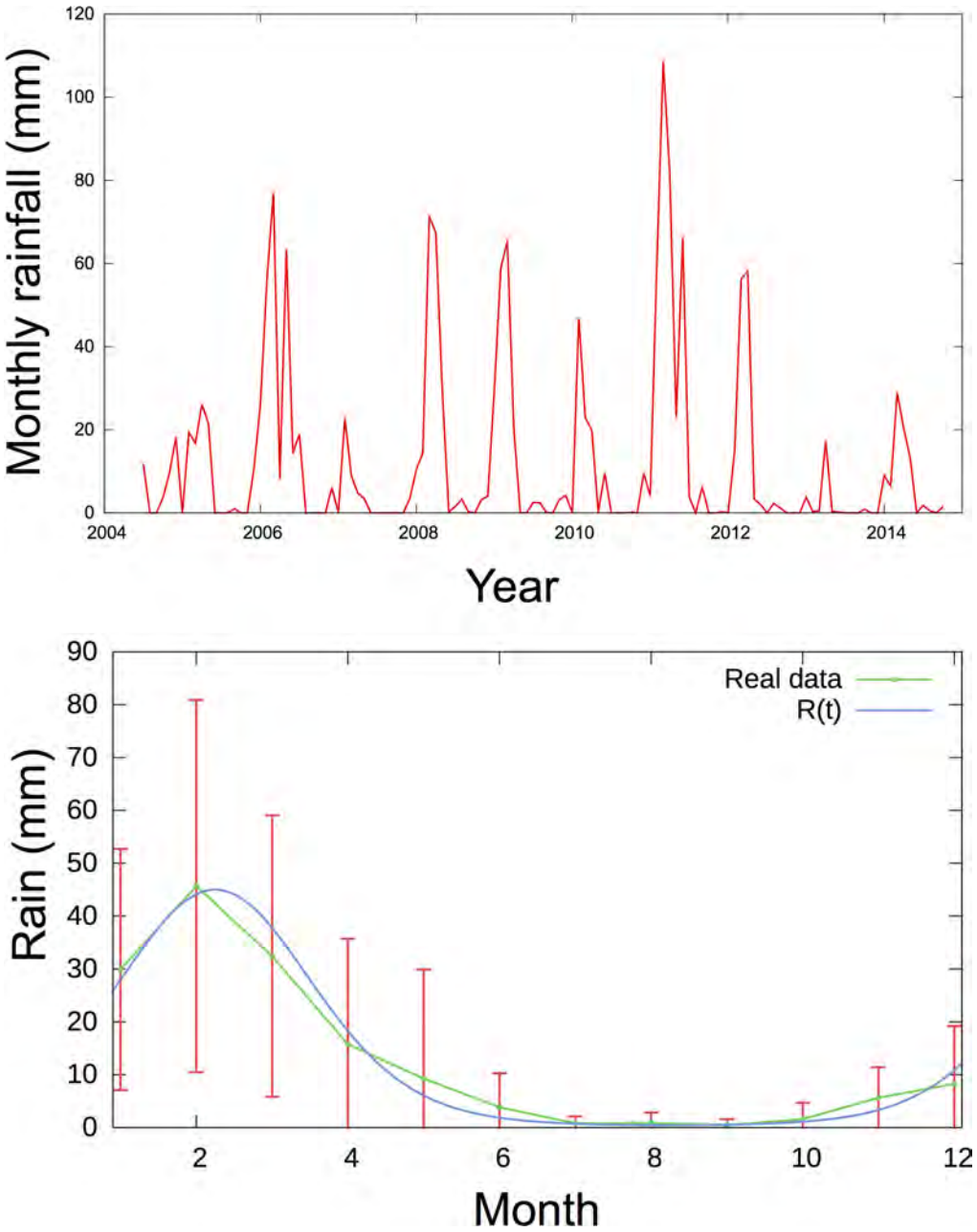

Extended Data Figure 5 | Rainfall data from NamibRand Nature Reserve. Top: 10-year time-series of monthly rainfall totals 2004–2014, averaged across multiple sites within NamibRand Nature Reserve (data provided by V. Hartung). Bottom: mean monthly rainfall (that is, averaged for each month across all years) in NamibRand Nature Reserve from 2004 to 2014 (green line, ± 1 s.d. in red) and proposed rainfall function (blue). The noise term included in $R_{\text{ainfall}}(t)$ (equation (5) in Methods) ensures that the rainfall function variability is high during the rainy season and low in the dry season, consistent with the data.

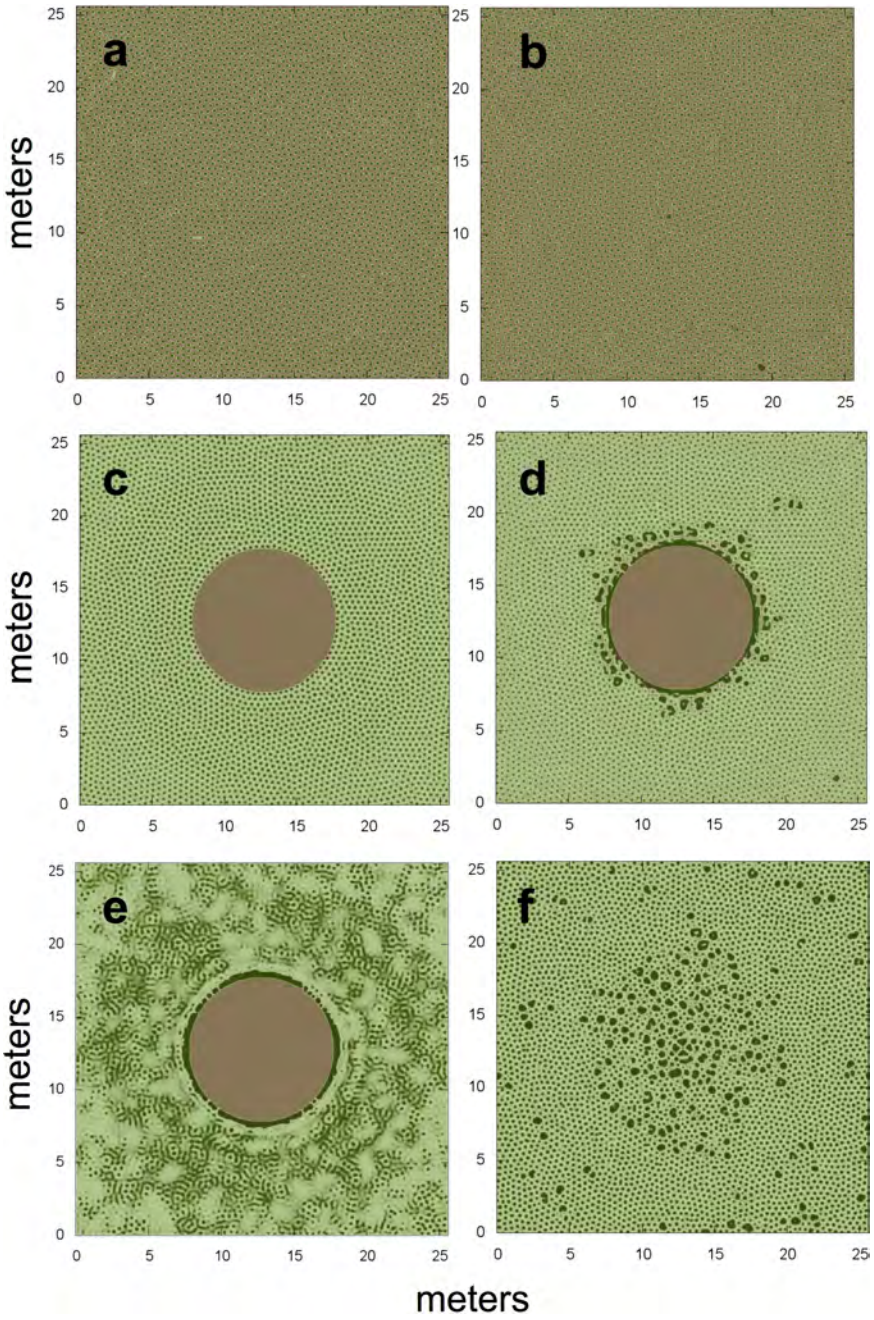

Extended Data Figure 6 | Vegetation dynamics with and without termite engineering. **a**, **b**, Comparison of the stationary pattern obtained with the vegetation model alone using (**a**) the original symmetric implementation for the root kernel and (**b**) the modified root kernel that is allowed to grow asymmetrically. **c**, **d**, Stationary pattern obtained with the naive setup (that is, one single, static colony in the centre of the system; constant rainfall); **c**, the resulting pattern using the original, symmetric root kernel; **d**, the pattern obtained when the asymmetric root system growth is implemented. **e**, **f**, Simulation run measuring the recovery time after the death of a colony in the coupled model with variable rainfall and asymmetric roots; **e**, system a few months before reaching stationarity; a ring of taller and denser vegetation is formed around the gap, and matrix vegetation is reaching its stationary clumpy distribution; **f**, several decades after colony death, the gap closes fully, and the remaining large matrix clumps disappear shortly thereafter. Brown, soil; green, vegetation. Colour intensity indicates vegetation density. Parameters are as in Extended Data Tables 1 and 2.

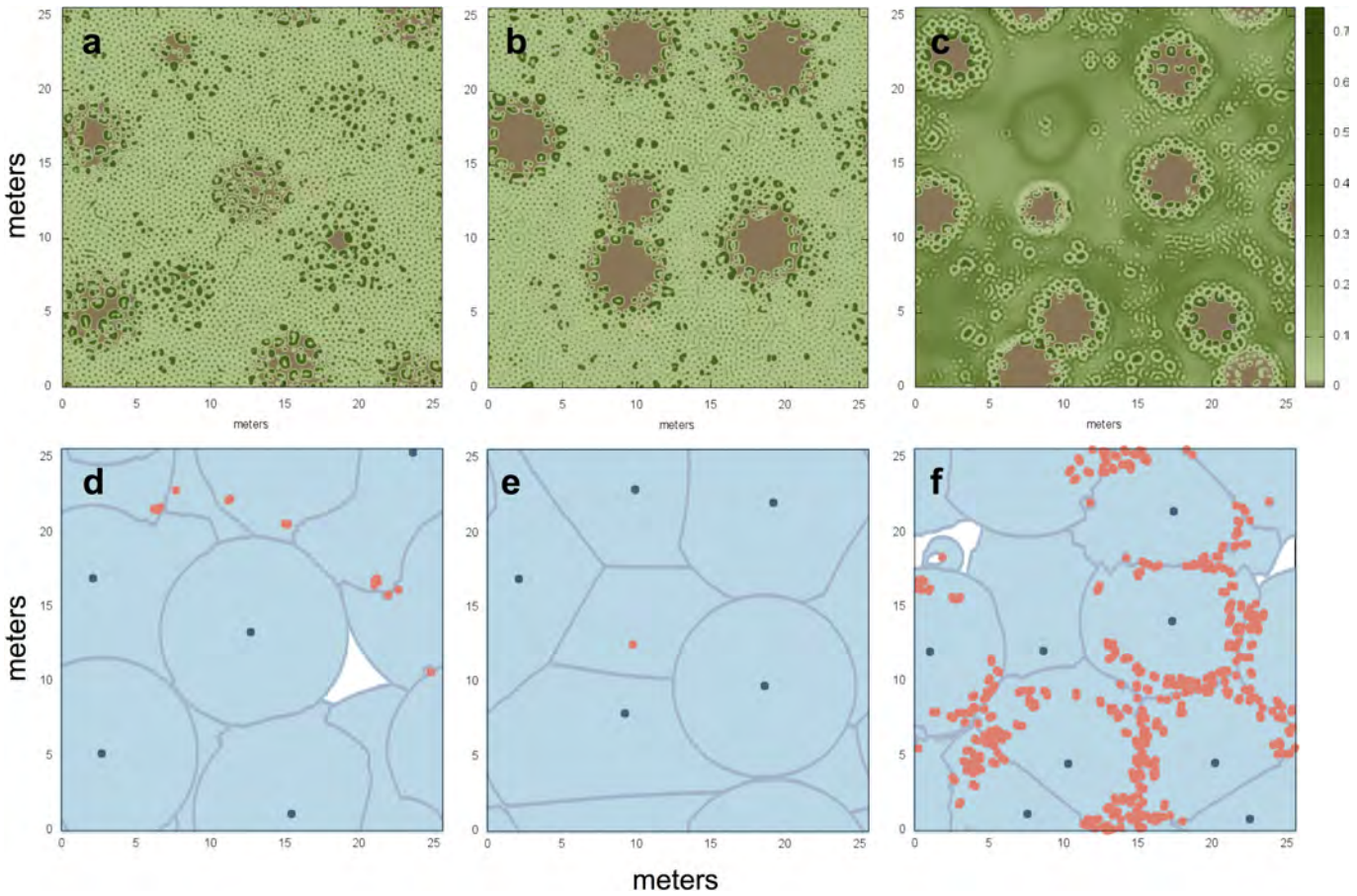

Extended Data Figure 7 | The effect of decreasing termite-induced plant mortality or increasing rainfall in the coupled system. When on-nest enhanced plant mortality is low and/or rainfall is high, vegetation growth outpaces termite engineering and, consequently, vegetation is found also on nests, disrupting (and for high enough rainfall values completely removing) the bare discs. **a**, Low mortality enhancement ($\nu = 1.1$); **b**, intermediate mortality enhancement ($\nu = 1.25$); values in **a** and **b** are both lower than in Extended Data Table 1 but have the same average rainfall as Extended Data Fig. 5; **c**, intermediate mortality enhancement ($\nu = 1.25$) and average rainfall increased by 10%. Brown, soil; green, vegetation. Colour intensity indicates vegetation density. **d**–**f**, Corresponding underlying termite territories and nests. Blue dots, established nests; red dots, incipient nests (including the initial diggings of an alate pair, leading to occasionally high local densities as shown in **f**). Snapshots taken for a peak in vegetation after the system has reached stationarity. Rest of the parameters as in Extended Data Tables 1 and 2.

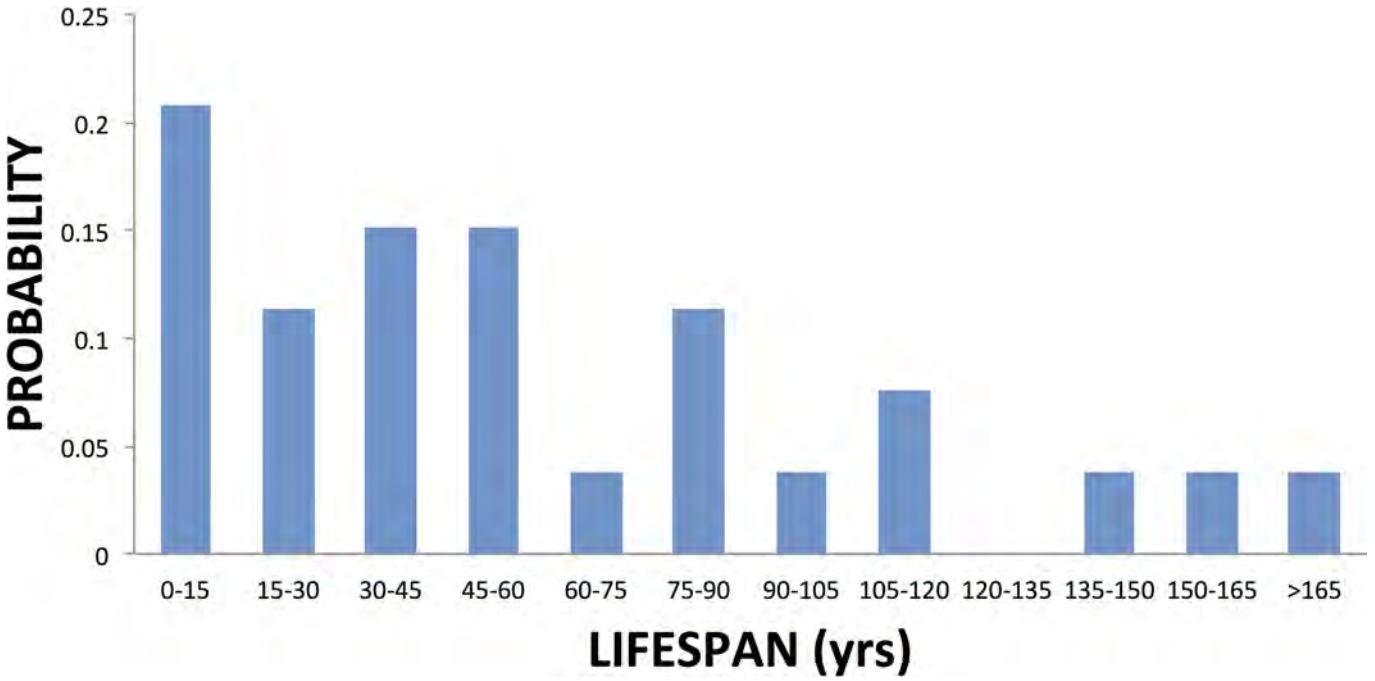

Extended Data Figure 8 | Distribution of FC lifetimes measured in the coupled model. For $n = 9$ replicates of the merged model, we kept track for ~300 years (until the end of the simulation) of 100 randomly selected FCs that were born after the stationary state (reached after ~100 years). Fifty-three of these FCs disappeared before the end of the simulation, allowing lifespan estimates for that subset. The resulting lifespans range from <5 years to >165 years, within reported estimates for Namibian FCs. Note that the distribution is truncated on the right tail owing to the limit of available simulation times; however, the overall shape of the distribution should not be strongly affected since such long-lasting FCs are very infrequent.

Extended Data Table 1 | List of parameters for the termite model and associated literature sources[7,29,31,35,37,44–54] and estimation procedures

Symbol	Description	Value	Units	Source
R_{max}	Maximum foraging radius	30	m	25-30m for subterranean termites and 15m for another Namib desert species in FC landscapes[44]; median distance of 35m for a desert rhinotermitid (*Heterotermes aureus*)[45]
B_{max}	Maximum possible colony biomass (carrying capacity)	$B_{ind}\times(2\times10^{6})$	g (termite)	Estimates for other Rhinotermitidae species from diverse habitats include >300,000 [46], >800,000 [47], to >2 and >3 million[48].
B_{mat}	Maturity/reproduction threshold	$B_{max}\times0.5$	g (termite)	Chosen as half B_{max} [31]. This choice does not influence results.
B_{ind}	Biomass of individual termite	2×10^{-3}	g (termite) individual^{-1}	Within weight range reported for various Rhinotermitidae spp.:[49-51].
c	Biomass conversion factor	0.07	g(termite) g^{-1}(res)	Tables 9.6-9.8 [50].
μ	Colony population birth rate	6.00	year^{-1}	Growth rate such that max size reached in 3 years (assumed to be smaller than that of largest colony species [31]).
m	Per capita worker natural mortality rate	1.00	year^{-1}	We assume the maximum lifetime of neuters ≈ 1 year [52].
P_{cst}	(Constant) vegetation density	Varied	Kg m^{-2}	Characteristic of arid and semi-arid environments[53].
m_C	Death rate of mature colonies	2.7	year^{-1}	Based on lifespan of ~25 years, which falls within the cross-taxa range for termites[37].
f_A	Alate production factor as proportion of $B_t(t)$	0.1	-	Within the cross-taxa range (0.012 – 1.42)[50] (their Table 9.7)
α	Reference value for conflict outcome probability	1.05	-	Unknown. Chosen to ensure that wars result in coexistence only when colonies have very similar sizes (based on the assumption that the war is a "war of attrition"[29,35,54]).
β	Shape factor for conflict outcome probability	150.00	-	
α_2	Reference value for conflict engagement probability	2.25	-	Unknown. Chosen to accentuate the difference in expansionistic tendencies as a function of colony size.
β_2	Shape factor for conflict engagement probability	10.00	-	
q	Shrinking factor for small winning colonies	0.1	-	Unknown. Chosen to be small but does not affect qualitative behavior.
A_{min}	Minimum viable area for a colony	$\pi\times0.1^2$	m^2	Arbitrary low number chosen for computational convenience.
f_m	Fraction of foraging territory occupied by mound proper	0.5	-	Approximate value based on data on foraging activity in *P. allocerus*[7].
ν	On-mound plant mortality enhancement	5.00	-	Chosen to simulate high mortality and low density of plants within fairy circles.
m_P	Vegetation mortality	10.00	year^{-1}	Chosen to fit tussock grasses for continuity with merged model (Extended Data Table 2).
N	Lateral grid size	1024	sites	Chosen for computational convenience.
dt	Integration time step	1	year	Chosen due to seasonality of the Namib desert
dx, dy	Mesh sizes	0.05	m	Chosen for computational convenience.

Extended Data Table 2 | List of parameters for the vegetation parts of the merged model and associated literature sources[9,10,15,55–60]

Symbol	Description	Value	Units	Source
K	Maximum standing biomass density	0.50	Kg m^{-2}	55
m_P	Vegetation natural mortality rate	10	$year^{-1}$	9
γ	Maximum infiltration rate	40	$year^{-1}$	15
Q	Infiltration half-saturation constant	0.1	Kg m^{-2}	15
W_0	Infiltration contrast between bare and vegetated soil	0.9	-	10,15
N	Soil water evaporation rate	4	$year^{-1}$	15
R_{educ}	Evaporation reduction due to shading	0.75	-	Within the range [10,15]
D_P	Seed dispersal coefficient	$3x10^{-3}$	$m^2 year^{-1}$	56,57
D_W	Soil water diffusivity	$5x10^{-3}$	$m^2 year^{-1}$	58; personal comm.: Ignacio Rodriguez-Iturbe.
D_O	Surface water diffusivity	0.00	$m^2 year^{-1}$	No topography + sandy soils (water infiltrates very quickly); personal comm.: Ignacio Rodriguez-Iturbe.
S_0	Minimal root system size	0.04	m	59
E	Root augmentation per unit biomass	4.0	Kg^{-1} m^2	60
Λ	Plant growth rate per unit soil water	0.25	Kg^{-1} $m^2 year^{-1}$	~10 times larger than value used for shrubs [15] since grasses grow more efficiently.
Γ	Soil water uptake per unit plant biomass	12	Kg^{-1} $m^2 year^{-1}$	9,60
R_0	Rainfall function reference parameter	54	mm $year^{-1}$	Chosen to match rainfall levels and variability shown by our data compilation.
ω	Rainfall function shape factor	1.0	-	
σ_R	Rainfall noise standard deviation	$2.5x10^{-3}$	mm $year^{-1}$	